

Hierarchical symmetry breaking in Moiré graphene domain-wall networks

Xue Yan¹, Kaiyun Chen², Yuan Yan¹, Fan Feng¹, Minglei Sun¹, Christan Brandl¹, Jefferson Zhe Liu^{1*}

¹ Department of Mechanical Engineering, The University of Melbourne, Parkville, VIC 3010, Australia

² Northwest Institute for Nonferrous Metal Research, Xi'an 710016, China

Email: zhe.liu@unimelb.edu.au

Abstract

Moiré network formation in graphene bilayers breaks stacking symmetry, giving rise to domain walls that host topologically protected one-dimensional states. Here we show that these systems undergo an additional symmetry breaking at the level of the domain-wall network geometry, leading to the spontaneous emergence of chiral network configurations that are not determined by topology alone. Using atomistic structural relaxation and electronic-structure calculations, we show that TDW networks adopt chiral geometries through lattice relaxation. Via developing a comprehensive phase diagram defined by strain and interlayer flexibility, we discover three equilibrium network morphologies: straight, mono-chiral, and dual-chiral. Chiral networks arise from the global minimization of TDW energy under moiré geometric constraints. Tight-binding calculations show that straight networks host junction-centred states, whereas chiral networks shift spectral weight toward asymmetric edge modes. While topologically protected states naturally emerge at AB/BA domain boundaries in moiré bilayers, we demonstrated that the localization of boundary states is network-symmetry dependent. Our results show that symmetry breaking at both the stacking and network levels provides a new way to understand and control low-energy electronic states in moiré bilayers.

Introduction

Moiré network formation in graphene bilayers is often described as long-wavelength superlattices^{1,2}, where it breaks stacking symmetry. The spatial modulation of interlayer registry induced by twist or strain, when combined with structural relaxation, partitions the bilayer into distinct stacking domains separated by topological domain walls (TDWs)^{3,4}. These domain walls are natural structural features of relaxed moiré systems and assemble into extended networks that host topologically protected one-dimensional boundary channels enforced by opposite valley Chern numbers of adjacent stacking domains⁵⁻⁷. As a result, TDW networks are widely regarded as central to the low-energy electronic reconstruction of relaxed Moiré systems^{4,6,8} and have been predominantly discussed within a topology-dominated framework⁹⁻¹¹. From this perspective, Moiré graphene can be naturally viewed as a symmetry-broken system in which electronic transport and localisation are governed by stacking domains and their connecting boundaries. However, although topology guarantees the existence of these one-dimensional boundary channels¹²⁻¹⁵, it does not uniquely determine the geometry of the networks that host them.

Moiré network geometry is not fixed by topology and represents another level of symmetry breaking. While topological considerations constrain the existence and connectivity of individual domain walls^{16,17}, they do not require the network itself to remain straight or symmetry-equivalent. Recent experiments reveal a qualitatively different regime in which TDW networks undergo pronounced geometric reconstruction, developing strongly curved and swirl-like morphologies that cannot be reconciled with an idealised network of straight, equivalent walls^{3,18-23}. Such curved TDW networks have been observed across a wide range of Moiré and interface-supported systems, including epitaxial graphene, graphene and blue phosphorus layers on metal substrates, and transition-metal dichalcogenide heterostructures. Their recurrence across different materials suggest that curved TDWs are unlikely to be accidental, but may instead reflect arise from a shared underlying mechanism governing network geometry. At the superlattice scale, these patterns reflect reduced symmetry in the network geometry²⁴. This raises a fundamental question: *if topology ensures the existence of domain-wall states but does not fix network geometry, what determines the curved network geometry under fixed Moiré constraints? And how does such network-level symmetry breaking reorganise the spatial distribution of boundary states?*

The TDWs in Moiré network are not only topological interfaces but also elastic line defects. They can be rigorously described as partial basal-plane dislocations characterized by a Burgers vector associated with interlayer translation²⁵⁻²⁷. Classical dislocation theory shows that the energy of a line defect depends on its orientation relative to the Burgers vector. Segments parallel to the Burgers vector carry lower elastic energy than perpendicular segments, which create significant in-plane dilation or compression²⁸⁻

³⁰. This orientation dependence implies that, although topology guarantees the existence of domain walls, it does not uniquely determine their geometry. An isolated TDW therefore tends to curve to increase its screw-like character and lower its elastic energy. In a connected Moiré network, however, domain walls are constrained by junction connectivity and the spacing imposed by the superlattice²⁸. The resulting network geometry thus emerges from a competition between orientation-dependent wall energetics and the connectivity constraints required by the superlattice.

Here, we show that network geometry is determined by a competition between elastic energy and topological constraints. Using atomistic structural relaxation together with large-scale tight-binding calculations, we map a phase diagram controlled by biaxial strain and interlayer flexibility. The balance between orientation-dependent domain-wall energy and the junction spacing imposed by the Moiré pattern stabilises three equilibrium morphologies: straight, mono-chiral and dual-chiral networks. Interlayer flexibility plays a key role by allowing out-of-plane lattice deformation to relax strain in edge-oriented segments and reduce the energy difference between edge- and screw-like walls, thereby weakening the tendency toward curvature. This change in geometry directly reorganises the low-energy electronic structure. Straight networks localise boundary states at junctions. Chiral networks redistribute electronic weight along extended domain-wall segments and shift transport from node-centred to channel-dominated behaviour. Topology guarantees boundary modes, but their spatial distribution is governed by network geometry. Our results show that network geometry can be used to control boundary states in moiré systems.

Results

Chiral TDW Networks in Graphene Moiré Superlattices. Here, we investigate how mechanical relaxation governs the geometry of topological domain wall (TDW) networks in strained graphene Moiré bilayers. Equilibrium structures are computed across a two-dimensional parameter space defined by biaxial misfit strain — representing isotropic in-plane lattice mismatch between the graphene layers — and bottom flexibility. The bottom flexibility is controlled by either allowing or constraining out-of-plane relaxation of the bottom layer, thereby mimicking substrate-pinned (z-rigid) or free-standing bilayers as in experiments (see Methods: Implementation of bottom flexibility and Fig. S1). All relaxed configurations are analyzed and visualized using our previously developed stacking-order index²⁹, which maps the local stacking order across the superlattice.

In strained graphene moiré bilayers, interlayer lattice mismatch generates a periodic superlattice of alternating AB and BA stacking domains separated by TDWs that intersect at AA-stacked topological crossing points (TCPs)²⁹. Upon structural relaxation, however, we find that the TDW network is not confined to the ideal moiré grid. Instead, TDWs deviate from straight configurations and develop curved morphologies (Fig. 1A). Around each TCP, the collective bending of adjacent TDWs defines a local chiral handedness, providing a geometric basis for classifying network chirality.

Within the strain–flexibility parameter space, three distinct TDW morphologies emerge. A straight configuration preserves the underlying graphene lattice symmetry, whereas two additional configurations — termed mono-chiral and dual-chiral — exhibit broken mirror and inversion symmetry (Fig. 1A). The specific topology is determined by how curvature is accommodated during relaxation. For mono-chiral topology, all the chiral handedness around TCP is in the same direction (R: right-handed), whereas in the dual-chiral case, the two chiral directions (L: left-handed, and R: right-handed) are alternating every second row in the network. In the z-rigid case, increasing strain first stabilises mono-chiral networks at 0.1%, followed by dual-chiral configurations at 0.2–0.24%. By contrast, when out-of-plane relaxation is permitted (z-free), the sequence reverses: dual-chiral networks appear at low strain, mono-chiral configurations at intermediate strain, and nearly straight TDWs at higher strain. Direct comparison at fixed strain highlights the decisive role of bottom layer flexibility. For example, at 0.24% strain, chirality is suppressed in the z-free system, whereas the z-rigid system remains dual-chiral.

These results demonstrate that TDW network topology is not uniquely determined by topology, but instead arises from the interplay between in-plane strain and interlayer mechanical flexibility. Together, these factors control how curvature is distributed across the network, thereby selecting between symmetry-preserving and symmetry-breaking chiral configurations.

To quantify TDW geometry, we introduce two descriptors. The chiral angle α measures the deviation of a TDW from the line connecting neighbouring TCPs (Fig. 1B–C), and the curvature localisation parameter R_c characterises the spatial concentration of bending along a wall (Fig. 1D). In mono-chiral networks, α is finite and nearly uniform, indicating consistent handedness across the lattice. In dual-chiral networks, curvature localises between TCPs of identical handedness, while walls connecting oppositely handed TCPs remain nearly straight. In straight networks, both α and R_c approach zero. To distinguish the two different types of TDWs in the mono-chiral and dual-chiral cases, we also introduce two additional chiral angle descriptors α' and α'' as shown in Fig. 1B–C.

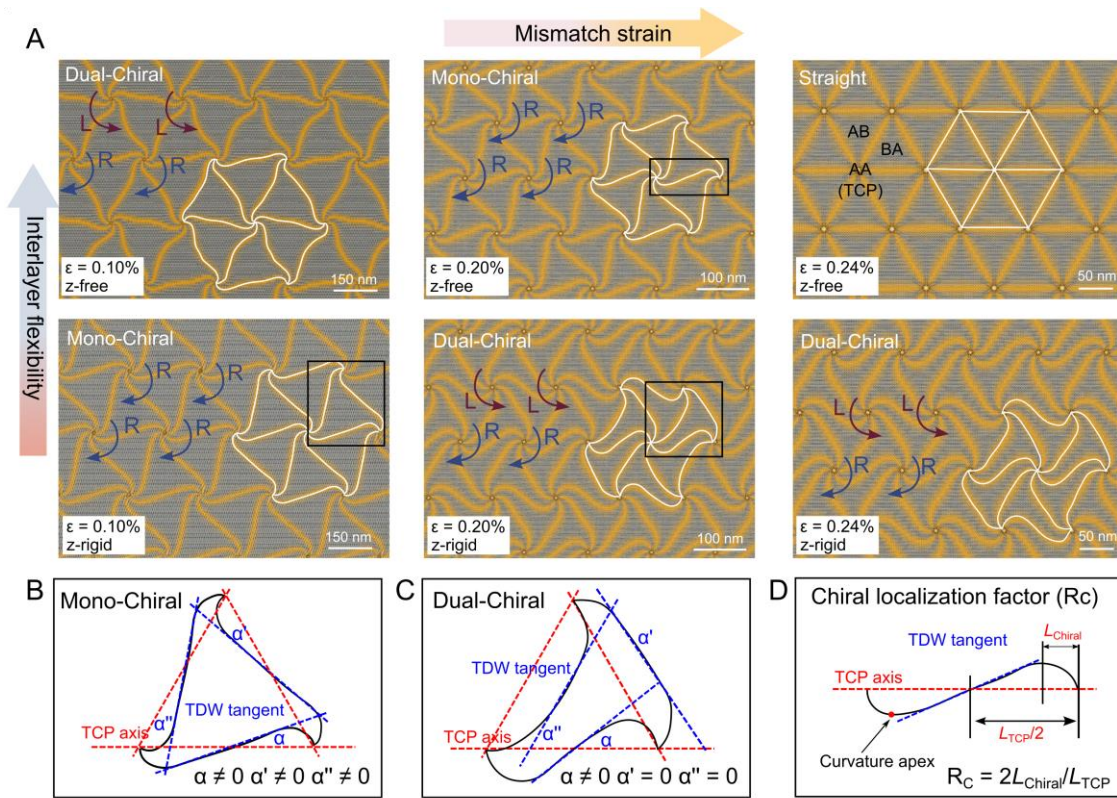


Fig. 1. Classification of TDW network morphologies and geometric descriptors of chirality. **A.** Representative moiré configurations organized by increasing biaxial misfit strain and interlayer flexibility. The stacking map is visualized using the stacking-order index²⁹. AB and BA stacking domains are shown in gray, while TDWs are highlighted in yellow connecting AA-stacked TCPs. **B–C.** Definition of the chiral angle α quantifies the deviation of a TDW from the axis connecting two neighboring TCPs at its midpoint. **D.** The curvature localization parameter R_c is defined as the distance from the curvature apex to the nearest TCP normalized by half of the TCP–TCP separation.

Strain–flexibility control of TDW network topology and symmetry. These descriptors define a phase diagram as a function of biaxial strain ϵ and bottom layer flexibility, quantified by the inverse bending stiffness $1/k$. Figure 2A maps the stable TDW morphologies identified at each point in this strain–flexibility space. Marker color represents the chiral angle α , and the angular sector represents the curvature localization parameter R_c . For each parameter set, the lowest-energy configuration is selected (see Methods: Configuration identification and Fig. S2). The phase map shows distinct TDW morphologies. At large strain ($\epsilon > 0.83\%$), TDWs adopt the straight configurations across the full range of flexibility, whereas at small strain ($\epsilon < 0.23\%$), only chiral morphologies are stable, where mono-chiral and dual-chiral networks appear in similar regions of the phase diagram (Fig. S3). Between these limits, bottom flexibility plays a decisive role in determining whether chirality persists. Highly flexible systems

transition to straight TDWs already near $\varepsilon \approx 0.23\%$, while rigid systems require substantially larger strain ($\varepsilon \approx 0.83\%$) to suppress chirality. At a fixed strain, increasing flexibility can therefore induce distinct morphological pathways, including dual-chiral \rightarrow mono-chiral \rightarrow straight (e.g., $\varepsilon = 0.30\%$) or direct dual-chiral \rightarrow straight transitions (e.g., $\varepsilon = 0.23\%$) (Fig. S4), showing that flexibility can independently influence TDW topology in a complicated and delicate way.

In Fig. 2A, within the chiral regime, the geometric descriptors α and R_c change systematically across the phase diagram. Both quantities initially increase with strain and subsequently decrease as they approach straight configurations. For example, along the z-rigid line ($k = 0^+$), R_c increases from $\varepsilon \approx 0.1\%$ to $\sim 0.8\%$, accompanied by a deepening of the dual-chiral (red) or mono-chiral (blue) colour that reflects increasing α . Beyond $\varepsilon \gtrsim 0.8\%$, both R_c and α collapse to zero as the system enters the straight-TDW regime. This behaviour reflects a progressive localisation and eventual suppression of curvature. Upon crossing into the straight-TDW regime, α and R_c drop abruptly to zero, indicating an abrupt loss of geometric chirality. Note that the variation of α and R_c with respect to strain and flexibility is not monotonic, particularly for $\varepsilon < \sim 0.2\%$. Overall, across the phase diagram, increasing strain suppresses TDW chirality, while greater bottom-layer flexibility lowers the strain needed to form straight walls. Chirality-driven changes in TDW geometry are accompanied by systematic modifications of the stacking topology.

Figure 2B quantifies the characteristic size of AA-stacked regions for the most energetically stable topology identified in each case. At equal strain, straight-wall configurations exhibit the largest AA domains with a radius of about 20 \AA , whereas both mono-chiral and dual-chiral networks significantly reduce the AA domain (a radius down to $\sim 10 \text{ \AA}$). The similar AA-domain sizes in mono-chiral and dual-chiral networks show that the reduction is caused by curvature itself rather than by its handedness. As strain increases, this contrast diminishes, consistent with the weakening of chirality near the transition to straight configurations.

Directional strain (anisotropic) provides an additional means to alter the TDW network topology beyond chirality. Under a biaxial isotropic loading (where no in-plane direction is preferred), dual-chiral TDW networks maintain nearly equivalent domain sizes (as seen in Fig. 1A) for all cases in the diagram (Fig. 2A). When strain becomes anisotropic, this in-plane domain geometric equivalence is broken. As seen in Fig. 2C, when a larger strain is applied along y direction, the distance between the neighboring TCP rows become unequal, leading to the splitting of previously symmetry-equivalent triangular domains into two inequivalent size groups. The TDW network remains dual-chiral, however, the directional loading drives

domains to adopt distinct shapes and characteristic dimensions. To quantify this effect, we introduce a domain geometry asymmetry parameter $A_d = 1 - d_1/d_2$, where d_1 and d_2 denote orthogonal domain dimensions. A_d approaches zero for geometrically symmetric domains. Under isotropic strain ($\varepsilon_{yy}/\varepsilon_{xx} = 1$ in Fig. 2C), A_d remains small (between zero and 0.15) and sporadic across the parameter space (Fig. S5). In contrast, under anisotropic strain ($\varepsilon_{yy}/\varepsilon_{xx} \neq 1$), domain geometry asymmetry becomes pronounced. As summarised in the phase map in Fig. 3C (right), pronounced domain geometry asymmetry appears only when directional strain, dual chirality, and sufficient interlayer flexibility are all present. A dashed boundary delineates the onset of domain asymmetry, separating the symmetric region ($A_d = 0$) from the symmetry-broken region ($A_d \neq 0$). Within the asymmetry regime, most A_d values range between 0.25 and 0.4, indicating a substantial deviation from the symmetric limit. The directional strain can induce another symmetry-breaking (i.e., breaking domain equivalence) and alter TDW network topology.

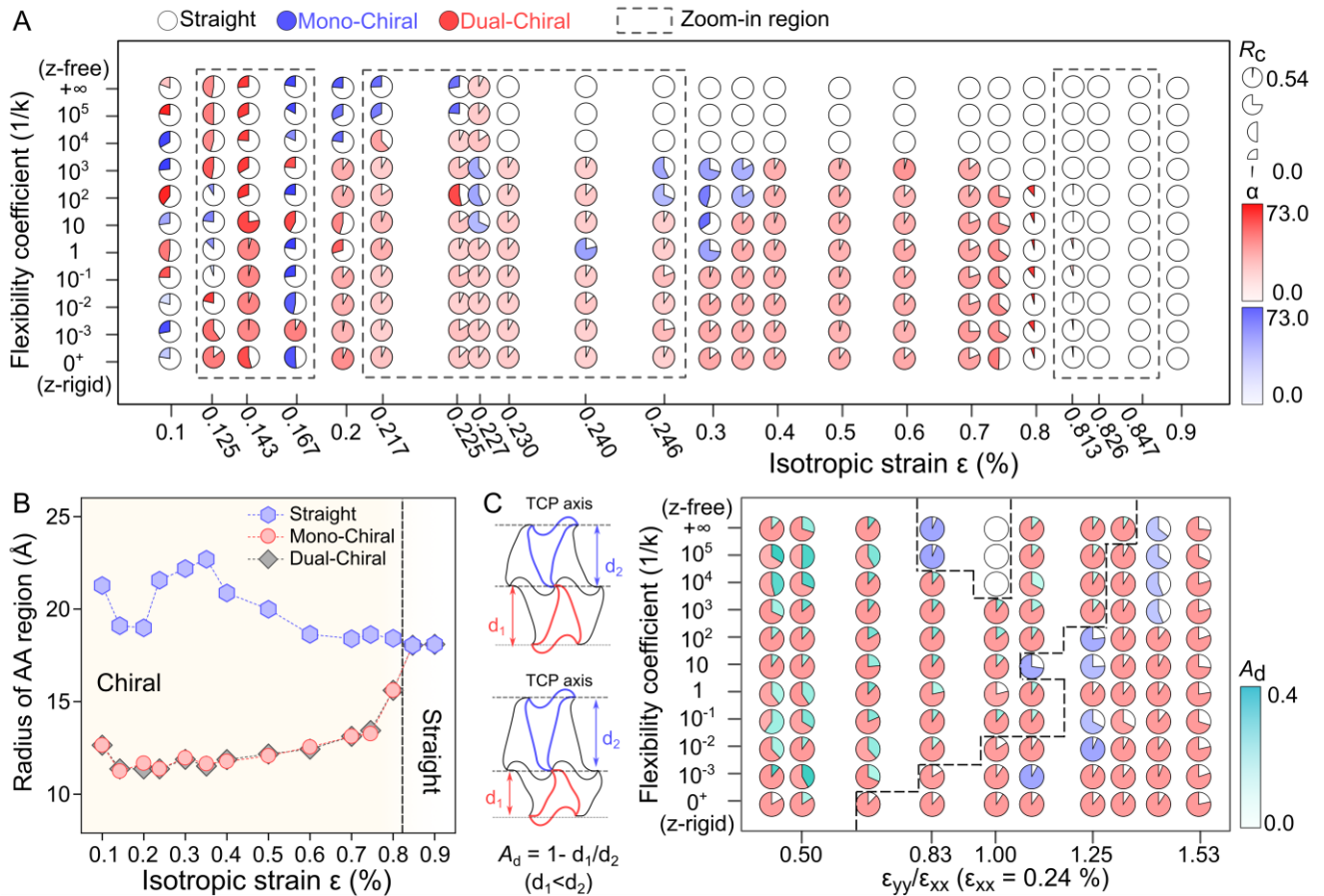


Fig. 2. Phase diagram of chiral TDW networks. **A.** Ground-state morphologies mapped in the biaxial strain–flexibility space. The flexibility coefficient is quantified as the inverse bending stiffness $1/k$. **B.** Characteristic size of AA-stacked regions for the most energetically stable topology identified in each case. Data are compiled over the full range of interlayer flexibility parameters. For a given strain, structures sharing the same topology exhibit essentially identical AA sizes, indicating that AA

size is governed by topology rather than flexibility. C. Left: Schematic definition of AB/BA domain-shape symmetry and the asymmetry descriptor A_d . Right: phase map of anisotropic strain and flexibility, with marker color encoding A_d .

Energetic origins for the observed TDW chirality. To understand why TDWs become chiral, we analyse individual domain walls using dislocation theory. Each TDW can be described as a partial dislocation line separating laterally shifted AB and BA domains. The orientation of its Burgers vector with respect to the dislocation line (TDW) determines the dislocation character. When the Burgers vector is perpendicular to the wall, the dislocation is edge-like, whereas walls aligned parallel to the Burgers vector approach a screw-like character, with intermediate orientations corresponding to mixed type^{25,26}. Figure 3A summarises the sensitive dependence of the TDW formation energy on the angle θ between the Burgers vector and the line, for rigid and flexible bottom layers, under three different strains $\varepsilon = 0.1\%$, 0.2% , and 0.24% . Generally, the TDW with a more screw-like character ($\theta \sim 0$) are energetically favoured over edge-like walls. For example, at $\varepsilon = 0.1\%$, the formation energy reduces from -50 eV/Å down to $\sqrt{2}00$ eV/Å. In isotropic elasticity, an edge-like dislocation generates larger strain energy because of its associated dilatational deformation (governed by an often larger bulk modulus), which is typically larger than the strain energy caused by shear deformation in an edge dislocation (governed by an often smaller shear modulus)³⁰.

The energy difference between edge- and screw-like TDWs depends on both strain and interlayer flexibility. The energy difference decreases monotonically from ~ 147 meV at 0.1% strain in the z-rigid case to ~ 38 meV at 0.24% strain under z-free conditions, with intermediate values spanning the corresponding rigid and flexible cases. This change in edge–screw energy contrast can explain the transition toward straight TDWs in the phase diagram of Fig. 2. To show how this mechanism works in a chiral network, we examine a representative TDW segment extracted from a mono-chiral configuration at 0.24% biaxial strain under z-rigid conditions (see Methods: TDW model and energy analysis), where chirality remains stable despite the relatively high strain. Figure 3B shows the local formation-energy density (*i.e.*, per length) along this curved TDW, using the orientation-dependent formation energy as shown in Fig. 3A. In a chiral wall, the local orientation varies continuously along the wall length, allowing segments near the curvature apex to acquire a more screw-like character. This reorientation lowers the local formation energy in these regions. Although curvature slightly increases the total wall length, the energy gained from adopting screw-like orientations outweighs this cost. TDW curvature, therefore, represents an energetic optimisation of wall orientation under network constraints, rather than a passive geometric effect. As strain or interlayer flexibility reduces the energy contrast between edge-

and screw-like walls, the driving force for curvature weakens, and the network becomes straighter and more symmetric.

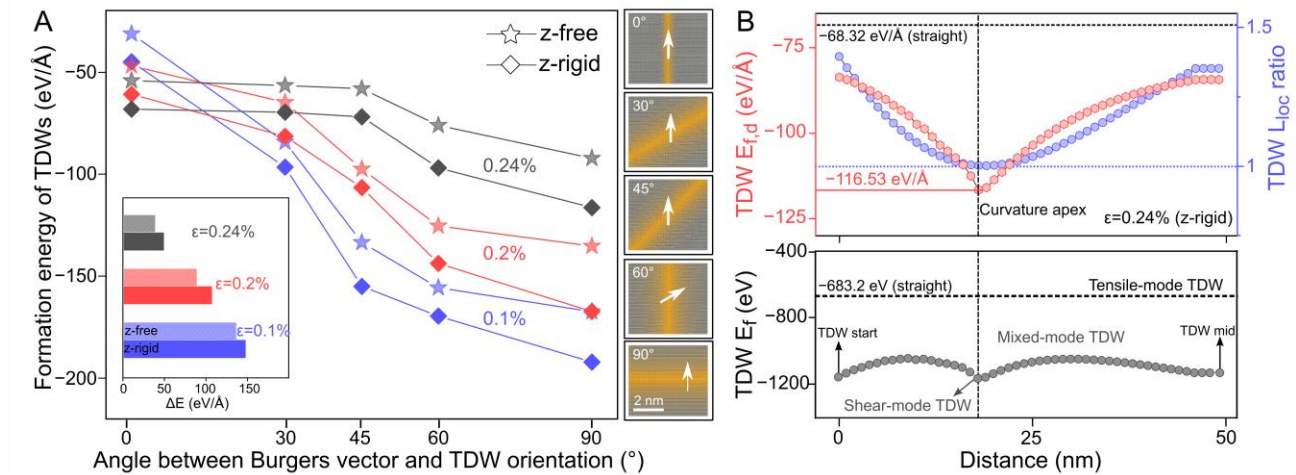


Fig. 3. Orientation-dependent formation energy of TDWs. **A.** Formation energy per unit length of TDWs as a function of the angle between the Burgers vector and TDW orientation under both z-rigid and z-free configurations. The inset compares the energy contrast between edge-like (0°) and screw-like (90°) TDW orientations. The schematic colormap illustrates representative orientation angles sampled in the calculations. **B.** Local formation-energy density (top) and the accumulated formation energy (bottom) along a TDW segment under 0.24% strain in the z-rigid configuration.

Emergent Chirality-induced Electronic Properties. To determine how geometric chirality reshapes low-energy electronic structure, we perform tight-binding calculations under a representative biaxial misfit strain of 0.20% with a z-rigid constraint (see Methods: Tight-binding calculation details). To directly probe spatial redistribution of electronic states, we compute the local density of states (LDOS) along trajectories crossing adjacent TDWs through a TCP. Spectra are extracted at TCP centres, AB and BA domain centres, TDW centres, and along TDW edges (Fig. 4), enabling a direct comparison between straight and chiral network geometries under identical strain conditions.

In straight TDW networks (Fig. 4A), electronic states near the Fermi level are strongly localized at AA-stacked junctions. These junctions host discrete bound states, including the characteristic -110 meV doublet previously reported in strained bilayer graphene¹⁹. Similar double-peak structures near the Dirac point have also been observed in twisted bilayer graphene, where they are associated with Van Hove singularities in the moiré superlattice³¹. The surrounding AB and BA domains exhibit a clear semiconducting gap, within which weak interference patterns appear as smooth spatial modulations,

Similar confined states within AB regions were reported in heterostrain-induced Moiré swirls ($\sim 0.1\%$ strain)¹⁹, where local density of states measurements revealed features reminiscent of a two-dimensional electron gas confined by hard walls³². Along straight TDWs, states near the Fermi level remain largely confined to junctions and wall centres. A small local gap persists at the TDW centre, while quasi-one-dimensional boundary modes emerge symmetrically along the two flanking edges, forming nearly mirror-balanced edge channels.

Introducing geometric chirality qualitatively reorganises this electronic landscape (Fig. 4B–C). Curved TDWs deform adjacent AB and BA domains, and this distortion is directly visible in LDOS maps: the smooth interference fringes of straight networks give way to fragmented, step-like modulations in chiral configurations. This modification reflects geometric distortion rather than a new electronic phase and appears consistently in both mono-chiral and dual-chiral networks. Simultaneously, spectral weight at AA junctions becomes weakened and spatially broadened, indicating enhanced hybridisation and a reduced effective size of AA regions in curved geometries (Fig. 4D). A comparable suppression of AA-centred peaks has been discussed in twisted bilayer graphene, where the double-peak structure near the Dirac point — commonly associated with Van Hove singularities — diminishes or becomes unresolvable at larger twist angles^{31,33,34}. Interpretations in that context include either the energy shift and broadening of Van Hove singularities beyond the accessible energy window³³ or a reduction in effective interlayer coupling, leading to spectra more reminiscent of decoupled monolayers³⁴. In parallel, spectral weight emerges near the Fermi level along the TDWs, signalling a partial closing of the local gap at wall centres and a redistribution of low-energy states away from junctions.

This geometric control becomes most striking in the behaviour of TDW edge modes (Fig. 4E). In straight networks, boundary modes appear only sufficiently far from TCPs and remain nearly symmetric between the two edges, aside from weak stacking-induced imbalance (Fig. S6). In contrast, chiral TDWs exhibit pronounced edge asymmetry that follows the local curvature. Near TCPs, spectral weight accumulates predominantly on the outer, high-curvature edge; approaching the curvature apex, this imbalance relaxes; farther along the wall, the dominant edge can even reverse. Curvature therefore acts not as a minor perturbation, but as a primary organising principle of boundary localisation. At the network scale, this asymmetry is further constrained by TDW connectivity and TCP handedness. In mono-chiral networks, TDWs connect TCPs of identical handedness, forcing inversion of the high-curvature edge between equivalent endpoints. In dual-chiral networks, opposite-handed TCPs impose a local mirror relation that preserves boundary localisation on the same physical side near both crossings (Fig. S7). Boundary modes are thus governed simultaneously by local curvature and global network chirality.

Together, these results reveal a key insight: while topology guarantees the existence of boundary modes, it does not determine their spatial arrangement. Geometric symmetry breaking at the network scale redistributes low-energy spectral weight, shifts localisation from AA junctions to TDW boundaries, and reorganises edge-channel connectivity in real space. In chiral moiré networks, electronic structure is not merely protected by topology — it is actively sculpted by geometry. Previous theoretical and experimental studies established that valley Chern numbers guarantee the existence of topological boundary modes in AB–BA interfaces⁹⁻¹¹, with spatial localisation largely attributed to local stacking geometry at wall centres or AA junctions. Here, under identical stacking and strain conditions, we show that mesoscale network curvature redistributes spectral weight away from junctions and reorganises localisation along TDW edges.

Our findings expand the conventional topological framework of moiré electronics by identifying network geometry as an active and programmable degree of freedom. Beyond the guaranteed existence of boundary states, we show that curvature and chirality can reorganise where and how these states localise, establishing geometry as a real-space control knob for electronic behaviour. This separation between topological protection and geometric distribution suggests new strategies for engineering anisotropic transport, programmable one-dimensional channels, and curvature-defined electronic architectures in moiré materials. More broadly, our work points toward a mesoscale design paradigm in which network topology, rather than only lattice symmetry or twist angle, becomes a fundamental parameter for controlling emergent electronic phenomena.

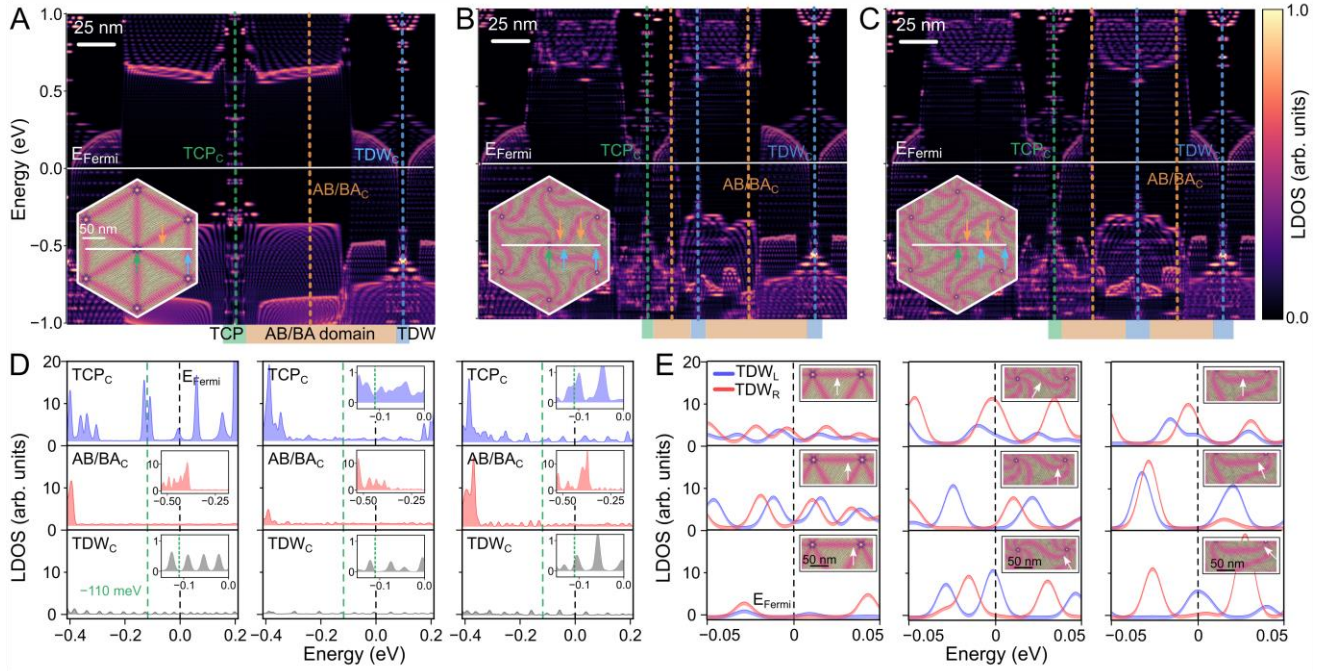


Fig. 4. Electronic structures of TDW networks. A-C. Spatially resolved LDOS along the white trajectories shown in the insets for straight (A), mono-chiral (B), and dual-chiral (C) TDWs under 0.20% biaxial misfit strain with a z-rigid constraint. **D.** LDOS spectra sampled at the corresponding marker positions in A–C. **E.** LDOS evolution along the TDW edge away from a TCP outward. The white arrow indicates the sampling direction from the left to the right TDW edge (TDW_L to TDW_R).

Discussion

TDW networks are often treated as collections of equivalent one-dimensional defects, with their geometry and electronic structure assumed to follow from an isolated wall. Most existing studies of TDWs have focused on local stacking registry, dislocation character, and the topological protection of boundary modes^{25,26}, implicitly assuming that network geometry simply follows from relaxation. Our results show that this picture is incomplete when TDWs are considered as connected elements within a deformable moiré lattice. Under mechanical relaxation, TDW networks can spontaneously enter chiral morphologies that break the symmetry of the straight configuration. This transition does not arise from a local instability of an individual domain wall. Instead, the formation energy of a TDW depends on its orientation relative to the Burgers vector. Curvature therefore redistributes line energy along the network. Because individual domain walls are connected through fixed junctions imposed by the moiré superlattice, such curvature cannot be optimized independently for each wall segment, and energy minimization must occur at the level of the entire network. This network-level optimization leads to symmetry breaking driven by elastic constraints rather than external forcing. The network selects its geometry collectively rather than through local instabilities. Importantly, symmetry breaking at the network level does not require the selection of a single global handedness. Instead, it refers to the removal of the constraint that favors a unique straight configuration, after which multiple symmetry-inequivalent network geometries, including mono-chiral and dual-chiral states, become energetically accessible.

Chirality therefore emerges as a network-level property that cannot be predicted from a single isolated wall.

Once realized, this symmetry-broken geometry changes the distribution of low-energy electronic states. In contrast to straight networks, where states remain largely junction-centered and boundary modes appear as nearly equivalent channels, chiral networks shift electronic localization toward domain-wall edges in a geometry- and connectivity-dependent manner. Boundary modes become spatially asymmetric, reflecting network handedness rather than only local stacking or valley topology. More broadly, these results suggest that similar symmetry breaking can arise when topological structures form connected networks in deformable materials^{21,22}, emphasizing the active role of geometry in shaping electronic topology. From a broader perspective, the emergence of chiral TDW networks in moiré bilayer graphene reflects a general mode of symmetry breaking in deformable interfacial systems^{3,23}, in which elastic relaxation and geometric constraints together favor a handed network configuration. Related geometry-driven symmetry lowering has been discussed in broader interface contexts²⁰, suggesting that network-level geometric symmetry breaking may also occur in other elastically compliant interface systems.

In summary, our work establishes TDW networks as collective geometric and mechanical objects, in which elasticity, topology, and global network geometry determine symmetry-broken morphologies and reorganize low-energy electronic states.

Methods

MD dynamics simulation details: Molecular dynamics (MD) simulations were performed using the LAMMPS package³⁵. Carbon-carbon interactions within each graphene layer were described by the REBO potential³⁶, while interlayer interactions were modeled using the registry-dependent Kolmogorov-Crespi potential³⁷. Periodic boundary conditions were applied in the in-plane (x - y) directions. MD simulations were carried out in the canonical ensemble (NVT) using a Nosé-Hoover thermostat³⁸. Mismatch-strained bilayer graphene supercells were constructed using different numbers of graphene unit cells in the bottom and top layers. A prescribed biaxial tensile strain was imposed by uniformly stretching the bottom layer, whereas the top layer was kept strain-free by adjusting its unit-cell number accordingly. To maintain a constant imposed strain, bottom-layer carbon atoms were constrained in the in-plane (x - y) directions throughout the simulation. For structural analysis and visualization, the local stacking configurations were characterized using the stacking order index²⁹. For each strain condition, the system was first energy-minimized and subsequently equilibrated using a multi-stage thermal annealing protocol: equilibration at 1 K, heating to 300 K followed by equilibration, and finally cooling back to 1 K. Each isothermal holding stage was simulated for 100 ns.

Configuration identification: For each parameter set (strain and interlayer flexibility), candidate configurations were generated using the thermal annealing protocol described above, starting from distinct initial stacking phases and/or modified out-of-plane constraint strengths to promote access to competing local minimum. All candidate configurations were subsequently re-equilibrated under identical simulation conditions. The total energies of these configurations were then directly compared, and the configuration with the lowest total energy was identified as the thermodynamically stable phase

for the given parameter set. Left- and right-handed mono-chiral TDW networks were both examined and found to be symmetry-related and energetically degenerate within numerical accuracy (Fig. S8). Consistent with previous studies based on nudged elastic band calculations¹⁹, no energetic preference between opposite handedness is expected in the absence of explicit symmetry-breaking fields.

Implementation of interlayer flexibility: To investigate the role of interlayer flexibility, different constraint schemes were applied to the bottom graphene layer. In the z-rigid case, bottom-layer atoms were fixed in all three spatial directions (x, y and z), representing a rigid substrate limit. In the z-free case, bottom-layer atoms were constrained only in the in-plane directions (x-y) to preserve the imposed strain, while remaining free to relax along the out-of-plane (z) direction. In addition, intermediate degrees of out-of-plane flexibility were modeled by applying a harmonic restraint along the z direction to bottom-layer atoms, with a tunable force constant k. This approach provides a continuous interpolation between the rigid and fully flexible limits and allows systematic control of interlayer flexibility. For simulations with controlled out-of-plane flexibility, a harmonic spring potential was applied to the z coordinate of bottom-layer carbon atoms,

$$V(z) = \frac{1}{2}k(z - z_0)^2 \quad (1)$$

where k is the spring constant and z_0 is the reference out-of-plane position. By varying k, the effective out-of-plane compliance ($\propto 1/k$) of the bottom layer could be tuned systematically. The limit $k \rightarrow \infty$ corresponds to the z-rigid case, while $k \rightarrow 0$ recovers the z-free limit.

TDW model and energy analysis: Dislocation structures were constructed within mismatch-strained bilayer graphene supercells by using different numbers of graphene unit cells in the top and bottom layers, thereby introducing a prescribed in-plane strain. The character of each dislocation was determined by the relative orientation between the graphene lattice shift direction (defined by the local carbon-atom displacement across the defect) and the dislocation line direction, allowing classification into tensile, shear, or mixed dislocations (Fig. S9). For mixed dislocations, the mixing angle was defined as the angle between the lattice shift direction and the dislocation line. The reference energy density of a uniformly strained, dislocation-free bilayer graphene system is defined as

$$\varepsilon_{ref} = \frac{E_0}{A_0} \quad (2)$$

where E_0 is the total energy of the strained bilayer graphene system without TDW and A_0 is the corresponding supercell area. The formation energy per unit length of a dislocation is then defined as

$$E_f = \frac{E_{TDW} - \varepsilon_{ref}A}{L} \quad (3)$$

where E_{TDW} is the total energy of the system containing the dislocation, A is the area of the corresponding supercell, and L is the dislocation length.

The orientation dependence of the dislocation formation energy was first obtained by fitting the formation energy per unit length E_f as a function of the dislocation orientation angle θ . For a curved TDW, the local formation-energy density was then evaluated by assigning to each point along the TDW a local line energy corresponding to its local orientation. Specifically, the local orientation angle $\theta(s)$ at position

along the TDW was determined from the local tangent direction of the dislocation line, and the local formation-energy density was defined as

$$E_{f,d}(s) = E_f(\theta(s)) \quad (4)$$

where $E_f(s)$ is the fitted orientation-dependent formation energy per unit length.

Tight-binding calculation details: Tight-binding (TB) calculations were performed using a Slater–Koster formalism³⁹ for carbon p_z orbitals, with all hopping parameters adopted from previously reported parametrizations⁴⁰. The in-plane nearest-neighbor π hopping and interlayer σ coupling were set to $\gamma_0 = 2.7$ eV and $\gamma_1 = 0.48$ eV, respectively, with interatomic hopping amplitudes described by distance-dependent exponential functions. Using this established TB parameter set, we first benchmarked the model against AB-stacked bilayer graphene (Fig. S10). To define a consistent energy reference, an overall onsite energy shift of -0.78 eV was applied uniformly to all atomic sites, such that the charge-neutrality point of AB-stacked bilayer graphene is reproduced within the tight-binding convention reported in the literature⁴¹. The local density of states (LDOS) was calculated from the TB eigenvalues and eigenstates using Gaussian broadening with a standard deviation of 5 meV. For LDOS maps along selected real-space paths, the LDOS was obtained by averaging over atoms within a finite transverse width around the path. We verified that varying the average width does not affect the qualitative features or energy-dependent trends (Fig. S11). All LDOS maps were normalized using the same global minimum and maximum to ensure a consistent relative intensity scale.

Data availability

All data generated in this study are included in the main text and the Supplementary Information. Further data, along with any code required for reproducing the figures, are available from the authors on reasonable request.

Acknowledgments

X.Y. acknowledges financial support from the Early Career Researcher Grant of the University of Melbourne. J.Z.L. acknowledges support from the Australian Research Council (ARC). This research was undertaken with the assistance of resources from the National Computational Infrastructure (NCI Australia), an NCRIS-enabled capability supported by the Australian Government. This work was supported by resources provided by the Pawsey Supercomputing Research Centre's Setonix Supercomputer (<https://doi.org/10.48569/18sb-8s43>), with funding from the Australian Government and the Government of Western Australia.

Author contributions

X.Y. conceived the project, carried out the calculations and analysis, and wrote the manuscript. J.Z.L. supervised the project and contributed to conceptual development, in-depth discussions, and manuscript preparation. C.B. contributed to theoretical discussions on dislocation theory and chiral interfaces.

All authors discussed the results and approved the final manuscript.

References

- 1 Nuckolls, K. P. & Yazdani, A. A microscopic perspective on moiré materials. *Nature Reviews Materials* **9**, 460–480 (2024).
- 2 Adak, P. C., Sinha, S., Agarwal, A. & Deshmukh, M. M. Tunable moiré materials for probing Berry physics and topology. *Nature Reviews Materials* **9**, 481–498 (2024).
- 3 Park, D. *et al.* Unconventional domain tessellations in moiré-of-moiré lattices. *Nature*, 1–8 (2025).
- 4 De Jong, T. A. *et al.* Low-energy electron microscopy contrast of stacking boundaries: Comparing twisted few-layer graphene and strained epitaxial graphene on silicon carbide. *Physical Review B* **107**, 075431 (2023).
- 5 Huang, S. *et al.* Topologically protected helical states in minimally twisted bilayer graphene. *Physical Review Letters* **121**, 037702 (2018).
- 6 Ju, L. *et al.* Topological valley transport at bilayer graphene domain walls. *Nature* **520**, 650–655 (2015).
- 7 Yin, L.-J., Jiang, H., Qiao, J.-B. & He, L. Direct imaging of topological edge states at a bilayer graphene domain wall. *Nature Communications* **7**, 11760 (2016).
- 8 Xu, S. *et al.* Giant oscillations in a triangular network of one-dimensional states in marginally twisted graphene. *Nature communications* **10**, 4008 (2019).
- 9 Martin, I., Blanter, Y. M. & Morpurgo, A. Topological confinement in bilayer graphene. *Physical Review Letters* **100**, 036804 (2008).
- 10 Qiao, Z., Jung, J., Niu, Q. & MacDonald, A. H. Electronic highways in bilayer graphene. *Nano Letters* **11**, 3453–3459 (2011).
- 11 Zhang, F., MacDonald, A. H. & Mele, E. J. Valley Chern numbers and boundary modes in gapped bilayer graphene. *Proceedings of the National Academy of Sciences* **110**, 10546–10551 (2013).
- 12 Su, L. *et al.* Domain-Selective 1D Moiré Engineering and Topological Transitions in Bilayer Graphene. *Nano Letters* **25**, 14060–14065 (2025).
- 13 Georgoulea, N. C., Caffrey, N. M. & Power, S. R. One-dimensional topological channels in heterostrained bilayer graphene. *Physical Review B* **109**, 035403 (2024).
- 14 Verbakel, J., Yao, Q., Sotthewes, K. & Zandvliet, H. Valley-protected one-dimensional states in small-angle twisted bilayer graphene. *Physical Review B* **103**, 165134 (2021).
- 15 Li, J. *et al.* Gate-controlled topological conducting channels in bilayer graphene. *Nature Nanotechnology* **11**, 1060–1065 (2016).
- 16 Hou, T. *et al.* Metallic network of topological domain walls. *Physical Review B* **101**, 201403 (2020).
- 17 Tsim, B., Nam, N. N. & Koshino, M. Perfect one-dimensional chiral states in biased twisted bilayer graphene. *Physical Review B* **101**, 125409 (2020).
- 18 Gutiérrez, C. *et al.* Imaging chiral symmetry breaking from Kekulé bond order in graphene. *Nature Physics* **12**, 950–958 (2016).

- 19 Mesple, F. *et al.* Giant atomic swirl in graphene bilayers with biaxial heterostrain. *Advanced Materials* **35**, 2306312 (2023).
- 20 Song, Y.-H. *et al.* Realization of large-area ultraflat chiral blue phosphorene. *Nature Communications* **15**, 1157 (2024).
- 21 Weston, A. *et al.* Atomic reconstruction in twisted bilayers of transition metal dichalcogenides. *Nature Nanotechnology* **15**, 592–597 (2020).
- 22 Enaldiev, V., Zólyomi, V., Yelgel, C., Magorrian, S. & Fal'Ko, V. Stacking domains and dislocation networks in marginally twisted bilayers of transition metal dichalcogenides. *Physical Review Letters* **124**, 206101 (2020).
- 23 Ko, K. *et al.* Operando electron microscopy investigation of polar domain dynamics in twisted van der Waals homobilayers. *Nature Materials* **22**, 992–998 (2023).
- 24 Hu, J. *et al.* Controlled alignment of supermoiré lattice in double-aligned graphene heterostructures. *Nature communications* **14**, 4142 (2023).
- 25 Butz, B. *et al.* Dislocations in bilayer graphene. *Nature* **505**, 533–537 (2014).
- 26 Alden, J. S. *et al.* Strain solitons and topological defects in bilayer graphene. *Proceedings of the National Academy of Sciences* **110**, 11256–11260 (2013).
- 27 Jiang, L. *et al.* Soliton-dependent plasmon reflection at bilayer graphene domain walls. *Nature Materials* **15**, 840–844 (2016).
- 28 Escudero, F., Guinea, F. & Zhan, Z. Geometrical properties of strained and twisted moir'e heterostructures. *arXiv preprint arXiv:2511.16219* (2025).
- 29 Endo, Y. *et al.* Dynamic topological domain walls driven by lithium intercalation in graphene. *Nature Nanotechnology* **18**, 1154–1161 (2023).
- 30 Hirth, J. P., Lothe, J. & Mura, T. Theory of dislocations. *Journal of Applied Mechanics* **50**, 476–477 (1983).
- 31 Li, G. *et al.* Observation of Van Hove singularities in twisted graphene layers. *Nature physics* **6**, 109–113 (2010).
- 32 Zheng, Q. *et al.* Tunable sample-wide electronic kagome lattice in low-angle twisted bilayer graphene. *Physical Review Letters* **129**, 076803 (2022).
- 33 Trambly de Laissardière, G., Mayou, D. & Magaud, L. Localization of Dirac electrons in rotated graphene bilayers. *Nano letters* **10**, 804–808 (2010).
- 34 Yan, W. *et al.* Angle dependent Van Hove singularities in slightly twisted graphene bilayer. *arXiv preprint arXiv:1206.5883* (2012).
- 35 Thompson, A. P. *et al.* LAMMPS—a flexible simulation tool for particle-based materials modeling at the atomic, meso, and continuum scales. *Computer Physics Communications* **271**, 108171 (2022).
- 36 Brenner, D. W. *et al.* A second-generation reactive empirical bondorder (REBO) potential energy expression for hydrocarbons. *Journal of Physics: Condensed Matter* **14**, 783 (2002).
- 37 Kolmogorov, A. N. & Crespi, V. H. Registry-dependent interlayer potential for graphitic systems. *Physical Review B—Condensed Matter and Materials Physics* **71**, 235415 (2005).
- 38 Martyna, G. J., Tobias, D. J. & Klein, M. L. Constant pressure molecular dynamics algorithms. *The Journal of Chemical Physics* **101**, 10.1063 (1994).
- 39 Slater, J. C. & Koster, G. F. Simplified LCAO method for the periodic potential problem. *Physical Review* **94**, 1498 (1954).
- 40 Brihuega, I. *et al.* Unraveling the intrinsic and robust nature of van Hove singularities in twisted bilayer graphene by scanning tunneling microscopy and theoretical analysis. *Physical Review Letters* **109**, 196802 (2012).

- 41 Jung, J. & MacDonald, A. H. Accurate tight-binding models for the π bands of bilayer graphene. *Physical Review B* **89**, 035405 (2014).